Evaluation of AC Resistance in Litz Wire Planar Spiral Coils for Wireless Power Transfer

Xiaona Wang[*],[***], Pan Sun[*], Qijun Deng[†], and Wengbin Wang[***]

[*]Institute of Electrical Engineering, Naval University of Engineering, Wuhan, China
[**]Department of Electrical Engineering and Applied Electronic Technology, Tsinghua University, Beijing, China
[†]Department of Automation, Wuhan University, Wuhan, China
[***]State Grid Jiangxi Electric Power Research Institute, Jiangxi Province, China

Abstract

A relatively high operating frequency is required for efficient wireless power transfer (WPT). However, the alternating current (AC) resistance of coils increases sharply with operating frequency, which possibly degrades overall efficiency. Hence, the evaluation of coil AC resistance is critical in selecting operating frequency to achieve good efficiency. For a Litz wire coil, AC resistance is attributed to the magnetic field, which leads to the skin effect, the proximity effect, and the corresponding conductive resistance and inductive resistance in the coil. A numerical calculation method based on the Biot–Savart law is proposed to calculate magnetic field strength over strands in Litz wire planar spiral coils to evaluate their AC resistance.   An optimized frequency can be found to achieve the maximum efficiency of a WPT system based on the predicted resistance. Sample coils are manufactured to verify the resistance analysis method. A prototype WPT system is set up to conduct the experiments. The experiments show that the proposed method can accurately predict the AC resistance of Litz wire planar spiral coils and the optimized operating frequency for maximum efficiency.

Key words: AC resistance, Biot–Savart law, Efficiency, Litz wire, Wireless power transfer

I. INTRODUCTION

A relatively high frequency, i.e., from a few tens of kHz to MHz, is commonly required for an efficient wireless power transfer (WPT) system [1]. A Litz wire composed of multiple isolated strands with a small diameter is used in WPT instead of a single copper wire with a larger diameter because the Litz wire provides small alternating current (AC) resistance and results in a high quality factor at a high operating frequency. However, the AC resistance of Litz wire coils increases sharply with operating frequency and probably cancels out the benefit resulting from high frequency. Hence, a formula that can predict efficiency based on the evaluation of frequency-dependent coil resistance should be developed.

AC resistance consists of two components, namely, the conductive and inductive components, which are attributed to the skin effect and proximity effect, respectively. Conductive resistance can be determined according to wire parameters and operating frequency, while induction evaluation involves the calculation of the magnetic field over strands in a Litz wire bundle [2]-[4]. Hence, field distribution should be determined first.

Although the strength of a field varies at different positions in the cross section of a spiral turn, its area squared average is commonly used to calculate induction resistance [2]-[4] because each strand occupies all the positions of every other strand that comprises the wire in an ideal Litz wire. Consequently, all the strands are equivalent with regard to their current and resistance evaluations. The total induction resistance is expressed as the product of a single strand and the number of strands inside a wire. The field distribution and area squared average field in a wire cross section have been investigated in many previous works [2]-[16]. Most of these works use analytical models to present the field over a cylinder strand, and Maxwell's equations are commonly

adopted as models to evaluate the magnetic field distribution of circular coils [2], [3], [5]-[12], whereas other works are based on finite element analysis (FEA) simulations [4], [14]. Reference [4] used FEA simulation to analyze the fields at the upper and lower positions of a Litz wire and considered their squared average to evaluate induction losses in a planar spiral coil. Reference [14] developed a FEA-based model to calculate the fields of elliptic coils. Although the area squared average field of various turns varies, it is assumed constant along the length in the same turn because of the approximate symmetry of spiral coils.

The current study aims to present a novel analytical model based on the Biot–Savart law instead of Maxwell's equations to evaluate the field distribution in turns of Litz wire planar spiral coils and to predict AC resistance under various frequencies. The efficiency of a WPT system can be predicted under various frequencies and the optimized frequency for maximum efficiency can be selected based on the predicted frequency-dependent resistance.

The rest of this paper is organized as follows. Section II analyzes the resistance components of planar spiral coils. Section III introduces a model based on the Biot–Savart law to analyze the magnetic field distribution over strands in Litz wire bundles of planar spiral coils. Section IV compares the resistances predicted using the proposed method and the reference method [2]. Four coil prototypes are constructed and their resistances under various frequencies are measured and compared with the predicted ones. Section V set up a two-coil WPT system to verify the efficiency of the proposed method based on the predicted resistance. The last section presents the conclusions of the study.

II. RESISTANCE COMPONENTS OF PLANAR SPIRAL COILS

A. Models of Planar Spiral Coils

The real schematic of a planar spiral coil is shown in Fig. 1(a), in which the inner radius is r_{in}, the outer radius is r_{out}, the space between adjacent turns is s, and the diameter of the Litz wire winding the coil is d_w.   In practice, the ratio of s/d_w is usually smaller than 3, and typical practical integrated spiral coils are built with $s \leq d_w$ [17]. When s is not significantly larger than d_w, the real coil can be simplified for analysis to the one shown in Fig. 1(b), which is composed of a few concentric turns. For the external magnetic analysis, the exposed turn is considered a cylinder with a diameter of d_w and a uniform current density in its cross section, whereas other turns that generate the external field are considered filament currents, which are depicted in Fig. 1(c).

Coil power loss under high frequencies is divided into two parts, namely, conductive and inductive. Conductive loss is associated with direct current (DC) resistance and the skin effect, whereas inductive loss is attributed to the proximity
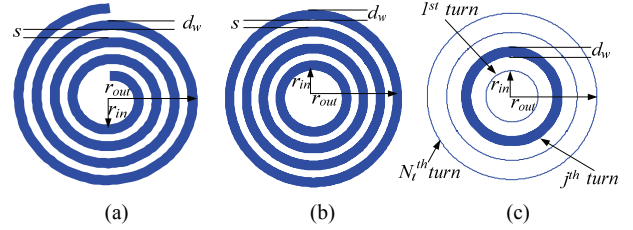

Fig. 1. Schematic of the planar solenoid coil: (a) Real model, (b) Simplified model, (c) Model for magnetic analysis.

effect that results from the magnetic field. Thus, two resistance components, namely, conductive resistance R_{cond} and inductive resistance R_{indu}, are used to reflect the corresponding losses. Consequently, total resistance R_0 is expressed by [2–14]

$$R_0 = R_{cond} + R_{indu}. \tag{1}$$

B. Conductive Resistance

The conductive resistance R_{cond} of a planar spiral coil with N_t turns is expressed by

$$R_{cond} = \sum_{j=1}^{N_t} \left(2\pi r_j R_{unit\_len\_cond} \right), \tag{2}$$

where r_j is the radius of the jth turn; and $R_{unit\_len\_cond}$ is the resistance per unit length in the planar spiral coil, which is wounded with a Litz wire with n_0 strands. $R_{unit\_len\_cond}$ is denoted as [2]

$$R_{unit\_len\_cond} = \frac{\xi \Phi_{cond}(\gamma)}{2\pi r_s n_0 \sigma}, \tag{3}$$

where ξ, $\Phi_{indu}(\gamma)$, and γ are calculated using (4), (5), and (6), respectively. ber, bei′, bei, and ber′ are Kelvin functions [18].

$$\xi = \frac{\sqrt{2}}{\delta} = \sqrt{\mu_0 \mu_r \sigma \omega}, \tag{4}$$

$$\Phi_{cond}(\gamma) = \frac{\text{ber}(\gamma)\text{bei}'(\gamma) - \text{bei}(\gamma)\text{ber}'(\gamma)}{\text{ber}'^2(\gamma) + \text{bei}'^2(\gamma)}, \tag{5}$$

$$\gamma = r_s \xi = r_s \sqrt{\mu_0 \mu_r \sigma \omega}, \tag{6}$$

where μ_0 is the free-space magnetic permeability ($\mu_0 = 4\pi \times 10^{-7}$ H/m), μ_r is the relative permeability ($\mu_0 = 1$ for free space), σ is the conductivity of the material and $\sigma = 5.8 \times 10^7$ $(\Omega m)^{-1}$ denotes copper, ω is the operating frequency, r_s is the radius of the Litz wire strand, and δ is the skin depth denoted by

$$\delta = \frac{\sqrt{2}}{\sqrt{\mu_0 \mu_r \sigma \omega}}. \tag{7}$$

C. Inductive Resistance

In an ideal Litz wire, all the strands inside it are assumed equivalent with respect to inductive loss because of azimuthal

and radial transpositions. In addition, the unit length loss $P_{unit\_len\_indu\_j}$ of a wire in a given turn j is assumed constant along the longitudinal direction. Thus, total inductive loss can be expressed by

$$P_{indu} = 2\pi \sum_{j=1}^{N_t} \left(r_j P_{unit\_len\_indu\_j} \right). \qquad (8)$$

Inductive loss can be associated with a sinusoidal current with an amplitude of I through the coil, which is expressed by

$$P_{indu} = I_{rms}^2 R_{indu} = \frac{1}{2} I^2 R_{indu}, \qquad (9)$$

where I_{rms} is the root mean square of I. Assuming the sinusoidal current amplitude is 1 A, (10) can be obtained as

$$R_{indu} = \frac{2P_{indu}}{I^2} = 2P_{indu}. \qquad (10)$$

With respect to the n_0 strands in the jth turn exposed to alternating magnetic field amplitudes $\mathbf{H_j}$ (with a norm of H_j), inductive loss per unit length is [2]

$$P_{unit\_len\_indu\_j} = n_0 \frac{-2\pi \gamma H_j^2 \Phi_{indu}(\gamma)}{\sigma}, \qquad (11)$$

where $\Phi_{indu}(\gamma)$ is expressed as follows:

$$\Phi_{indu}(\gamma) = \frac{ber_2(\gamma)ber'(\gamma) + bei_2(\gamma)bei'(\gamma)}{ber^2(\gamma) + bei^2(\gamma)}, \qquad (12)$$

where r_s is the radius of the strand, and ber^2 and bei^2 are Kelvin functions [18].

The integration of (1), (2), (3), (8), (10), and (11) yields

$$
\begin{aligned}
R_0 &= R_{cond} + R_{indu} \\
&= \sum_{j=1}^{N_t} \left(2\pi r_j \frac{\xi \Phi_{cond}(\gamma)}{2\pi r_s n_0 \sigma} \right) + 4\pi \sum_{j=1}^{N_t} \left(r_j n_0 \frac{-2\pi \gamma H_j^2 \Phi_{indu}(\gamma)}{\sigma} \right). \\
&= \frac{\xi \Phi_{cond}(\gamma)}{r_s n_0 \sigma} \sum_{j=1}^{N_t} r_j + \frac{8 n_0 \gamma \pi^2 \Phi_{indu}(\gamma)}{\sigma} \sum_{j=1}^{N_t} \left(-r_j H_j^2 \right)
\end{aligned} \qquad (13)
$$

Field strength varies at different positions within the cross section of a Litz wire bundle even in the same turn. However, the area average squared field in the respective cross section is commonly used to calculate losses [2–14]. The subsequent section details the evaluation of this average squared field for planar spiral coils.

III. FIELD DISTRIBUTION ANALYSIS OF PLANAR SPIRAL COILS

A. Area Average Squared Field

Fig. 2 shows the profile of magnetic field strength calculation, where r_b is the radius of the Litz wire bundle, namely, $d_w = 2r_b$. Point P inside the cross section of the jth turn of the coil can be expressed by the polar and Cartesian coordinate systems, namely, $P(j,\rho,\varphi)$ and $P(j,0,y,z)$, respectively. P is assumed to lie on the yz plane, i.e., $x = 0$ for P because of the symmetry of the planar spiral coil. Thus, the following is obtained:
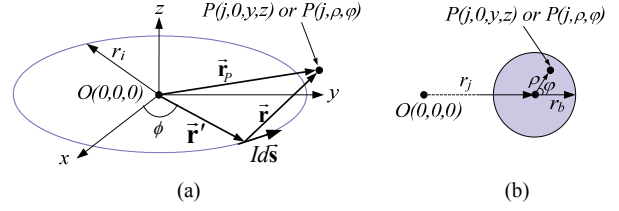

Fig. 2. Profile of magnetic field strength calculation: (a) Profile in the 3D coordinates, (b) Profile on the yz plane.

$$
\begin{aligned}
x &= 0 \\
y &= r_j + \rho \cos\varphi \\
z &= \rho \sin\varphi
\end{aligned} \qquad (14)
$$

The area average squared field in the jth turn of a planar spiral coil can be expressed by

$$H_j^2 = \frac{1}{\pi r_b^2} \int_{r=0}^{r_b} \int_{\varphi=0}^{2\pi} H_{j(\rho,\varphi)}^2 r\, dr\, d\varphi, \qquad (15)$$

where $H_{j(\rho,\varphi)}$ is the norm of the field strength $\mathbf{H}_{j(\rho,\varphi)}$ at the polar system point $P(j,\rho,\varphi)$, and the squared field in the cross section can be denoted by

$$H_{j(\rho,\varphi)}^2 = H_{j(\rho,\varphi)\_y}^2 + H_{j(\rho,\varphi)\_z}^2, \qquad (16)$$

where $H_{j(\rho,\varphi)\_y}$ and $H_{j(\rho,\varphi)\_z}$ are the norms of $\mathbf{H}_{j(\rho,\varphi)}$ in y-axis and z-axis directions, respectively. $\mathbf{H}_{j(\rho,\varphi)}$ is the field generated by all turns; hence, the following is obtained:

$$
\begin{aligned}
H_{j(\rho,\varphi)\_y} &= \sum_{i=1}^{N_t} H_{i\_j(\rho,\varphi)\_y} \\
H_{j(\rho,\varphi)\_z} &= \sum_{i=1}^{N_t} H_{i\_j(\rho,\varphi)\_z}
\end{aligned}, \qquad (17)
$$

where $H_{i\_j(\rho,\varphi)\_y}$ and $H_{i\_j(\rho,\varphi)\_z}$ are the norms of the field components over P due to i^{th} turn in the y-axis and z-axis directions, respectively. The following subsection focuses on the analysis of $H_{i\_j(\rho,\varphi)\_y}$ and $H_{i\_j(\rho,\varphi)\_z}$.

B. Magnetic Field Strength due to Other Turns

As shown in Fig. 2(a), the vector $\vec{r}_P$ that points from the Cartesian origin to P is

$$\vec{r}_P = y\hat{\mathbf{j}} + z\hat{\mathbf{k}}, \qquad (18)$$

where $\hat{\mathbf{j}}$ and $\hat{\mathbf{k}}$ are the unit vectors in the y-axis and z-axis, respectively. The differential current element is denoted by

$$Id\vec{\mathbf{s}} = Ir_i d\phi(-\sin\phi\hat{\mathbf{i}} + \cos\phi\hat{\mathbf{j}}), \qquad (19)$$

where $\hat{\mathbf{i}}$ is the unit vector in the x-axis, and its position is described by

$$\vec{\mathbf{r}}' = r_i(\cos\phi\hat{\mathbf{i}} + \sin\phi\hat{\mathbf{j}}). \qquad (20)$$

Thus, the corresponding relative position vector that points from $Id\vec{\mathbf{s}}$ to P is

$$\vec{\mathbf{r}} = \vec{\mathbf{r}}_P - \vec{\mathbf{r}}' = -r_i \cos\phi\hat{\mathbf{i}} + (y - r_i \sin\phi)\hat{\mathbf{j}} + z\hat{\mathbf{k}}, \qquad (21)$$

which leads to the following magnitude:

$$r = |\vec{\mathbf{r}}| = \sqrt{(-r_i \cos\phi\hat{\mathbf{i}})^2 + (y - r_i \sin\phi)^2 + z^2} \quad , \qquad (22)$$
$$= \sqrt{r_i^2 + y^2 + z^2 - 2yr_i \sin\phi}$$

and unit vector

$$\hat{\mathbf{r}} = \frac{\vec{\mathbf{r}}}{r} = \frac{-r_i \cos\phi\hat{\mathbf{i}} + (y - r_i \sin\phi)\hat{\mathbf{j}} + z\vec{\mathbf{k}}}{\sqrt{r_i^2 + y^2 + z^2 - 2yr_i \sin\phi}} \quad . \qquad (23)$$

Thus, the cross product of $Id\vec{\mathbf{s}} \times \hat{\mathbf{r}}$ is obtained as follows:

$$Id\vec{\mathbf{s}} \times \hat{\mathbf{r}} = Ir_i d\phi(-\sin\phi\hat{\mathbf{i}} + \cos\phi\hat{\mathbf{j}}) \times \frac{-r_i \cos\phi\hat{\mathbf{i}} + (y - r_i \sin\phi)\hat{\mathbf{j}} + z\vec{\mathbf{k}}}{\sqrt{r_i^2 + y^2 + z^2 - 2yr_i \sin\phi}}$$
$$= Ir_i d\phi[(z\cos\phi\hat{\mathbf{i}} + z\sin\phi\hat{\mathbf{j}} + (r_i - y\sin\phi)\hat{\mathbf{k}}] \qquad (24)$$

In accordance with the Biot–Savart law, the differential element of the magnetic field strength due to the current element $Id\vec{s} \times \hat{\mathbf{r}}$ at P is

$$d\vec{\mathbf{H}}_{i\_j(r_n,\varphi)} = \frac{\mu_r I}{4\pi} \frac{d\vec{\mathbf{s}} \times \hat{\mathbf{r}}}{r^2} = \frac{\mu_0 Ir_i}{4\pi} \frac{z\cos\phi\hat{\mathbf{i}} + z\sin\phi\hat{j} + (r_i - y\sin\phi)\hat{k}}{\left(\sqrt{r_i^2 + y^2 + z^2 - 2yr_i \sin\phi}\right)^3} d\phi \, , \quad (25)$$

where μ_r is the relative permeability, and $\mu_r = 1$ for free space. Thus, the field strength at P is

$$\vec{\mathbf{H}}_{i\_j(r_n,\varphi)} = \frac{\mu_r Ir_i}{4\pi} \int_0^{2\pi} \frac{z\cos\phi\hat{\mathbf{i}} + z\sin\phi\hat{j} + (r_i - y\sin\phi)\hat{k}}{\left(\sqrt{r_i^2 + y^2 + z^2 - 2yr_i \sin\phi}\right)^3} d\phi \quad . \quad (26)$$

Accordingly, three norms of field components are obtained in the x-axis, y-axis, and z-axis directions as follows:

$$H_{i\_j(\rho,\varphi)\_x} = \frac{\mu_r Ir_i}{4\pi} \int_0^{2\pi} \frac{z\cos\phi}{\left(\sqrt{r_i^2 + y^2 + z^2 - 2yr_i \sin\phi}\right)^3} d\phi = 0$$

$$H_{i\_j(\rho,\varphi)\_y} = \frac{\mu_r Ir_i}{4\pi} \int_0^{2\pi} \frac{z\sin\phi}{\left(\sqrt{r_i^2 + y^2 + z^2 - 2yr_i \sin\phi}\right)^3} d\phi$$

$$H_{i\_j(\rho,\varphi)\_z} = \frac{\mu_r Ir_i}{4\pi} \int_0^{2\pi} \frac{r_i - y\sin\phi}{\left(\sqrt{r_i^2 + y^2 + z^2 - 2yr_i \sin\phi}\right)^3} d\phi$$

$$\qquad (27)$$

$$i \neq j$$

C. Magnetic Field Strength due to Neighboring Strands

In addition to the field caused by other turns, the field created by neighboring strands in the same turn also contributes to the total field. The magnetic field in a strand situated at position ρ (Fig. 2(b)) can be derived as follows using Ampère's law based on the method introduced in Reference [2]:

$$H_{i\_j(\rho,\varphi)} = \frac{\mu_r I}{2\pi r_b^2}\rho \qquad (i = j) \, . \qquad (28)$$

Thus, the components in the y-axis and z-axis directions are

Coil no.	n_0	N_t	r_0 (mm)	r_b (mm)	r_{int} (mm)	r_{out} (mm)
I	20	23	0.25	1.5	25	105
II	31	23	0.2	1.5	25	105
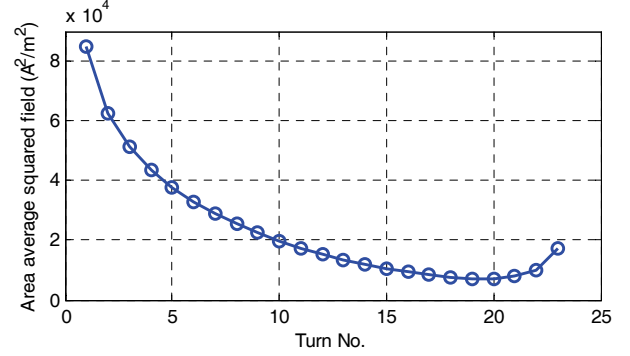
Fig. 3. Area average squared field vs. turn number.

$$H_{i\_j(\rho,\varphi)\_y} = \frac{\mu_r I}{2\pi r_b^2}\rho \cos\varphi$$

$$H_{i\_j(\rho,\varphi)\_z} = \frac{\mu_r I}{2\pi r_b^2}\rho \sin\varphi \quad . \qquad (29)$$

$$i = j$$

Equations (27) and (29) provide the comprehensive expression for the fields generated by all the turns at point P.

IV. EXPERIMENTAL VERIFICATION FOR COIL RESISTANCE

A. Predicted Resistance Compared with a Previous Work

Reference [2] plotted the predicted resistances according to Maxwell's equations and measured the ones for the two coils whose parameters are listed in Table I. Equations (15) to (29) show that the field is dependent on neither the radius nor number of strands. Thus, the respective turns of coils "I" and "II" are exposed to the same area average squared field. MATLAB simulation codes are developed based on the proposed method to evaluate field and resistance under various frequencies. Fig. 3 plots the area average squared field for various turns. It shows that the innermost turn (i.e., the first one) is exposed to the highest field, and the smallest area average squared field occurs at the 20th turn because the external fields due to other turns can partly cancel one another for the middle turns (e.g., the 5th turn until the 20th turn).

Fig. 4 depicts the resistances from Reference [2] and the predicted ones from the proposed method based on the Biot–Savart law. The length of strands is longer than that of the Litz wire because of strand twists. Hence, an additional 3.5% correction is added to the predicted resistances [4]. The resistances predicted using the proposed method agree well
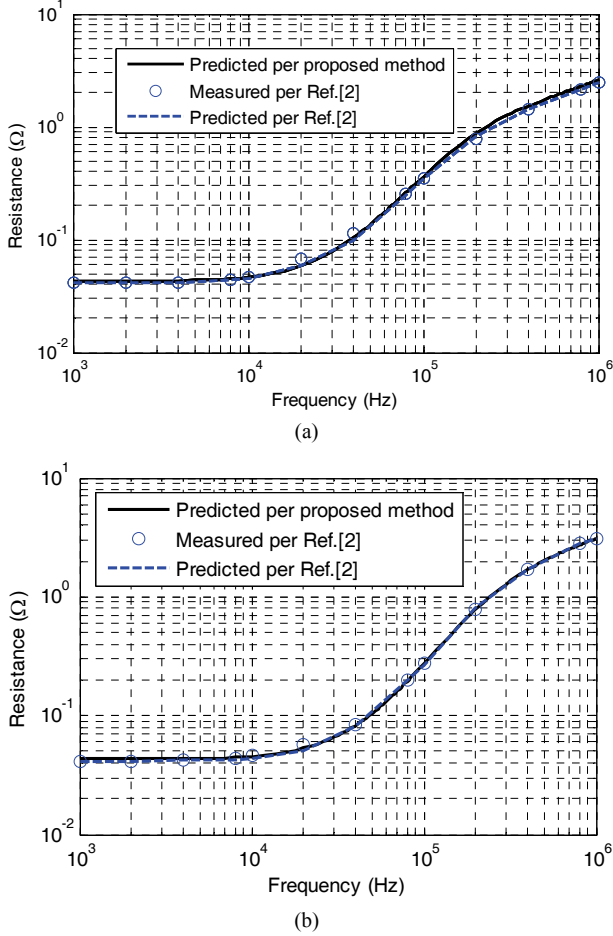
(a)

(b)

Fig. 4. Comparison of the predicted resistances with those from [2]: (a) Coil I (n_0 = 20 strands), (b) Coil II (n_0 = 31 strands). Measured from Ref. [2] indicates the measured resistances listed in Ref. [2] for coils with the same dimensions that corresponds to coils I and II.
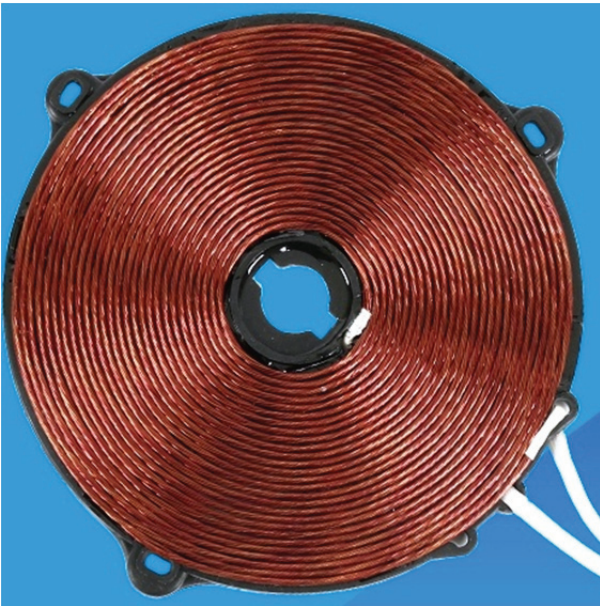

Fig. 5. Prototype of coils.

TABLE II
PARAMETERS OF THE FOUR LITZ WIRE   PLANAR SPIRAL PROTOTYPE COILS

Coil no.	n_0	N_t	r_0 (mm)	r_b (mm)	r_{int} (mm)	R_{out} (mm)
III	14	27	0.14	0.6	23	71
IV	20	28	0.13	0.5	23	78
V	40	27	0.05	0.38	23	71
VI	100	27	0.05	0.61	23	71

with those predicted in [2], although they have slightly higher values at the middle frequencies (i.e., 10–100 kHz) for both coils.

B. Resistances of Prototype Coils

Four prototype coils are manufactured for resistance measurements, and the picture of one is shown in Fig. 5. The parameters of these prototype coils are listed in Table II. Fig. 6 depicts the predicted and measured resistances versus the frequencies of these coils. All the resistances in this study are measured using an Agilent E4980APrecision LCR meter. The proposed method can predict AC resistance at low and high frequencies. For the middle frequency bands (i.e., 40–300 kHz, 30–300 kHz, 200–700 kHz, and 200–700 kHz for coils III, IV, V, and VI, respectively), the measured resistances are slightly higher than the predicted ones. In addition, the middle frequency bands move to higher frequencies with decreasing strand radius.

V. EXPERIMENTAL VERIFICATION FOR WPT EFFICIENCY

A. Efficiency Simulation for Series–Series Compensation WPT

Assume that three frequencies, namely, the operating frequency and the self-resonant frequencies at both sides, are the same for the simulation in the study. The self-resonant frequencies are regulated by adjusting the resonant capacitance while the resonant inductance remains constant. When the loss in capacitors is disregarded, the transfer efficiency for a two-coil structure WPT system with a series–series compensation inverter is [1]

$$\eta = \frac{\left(\dfrac{\omega M}{R_0+r}\right)^2}{1+\left(\dfrac{\omega M}{R_0+r}\right)^2+\dfrac{R_L}{R_0+r}} \times \frac{\dfrac{R_L}{R_0+r}}{1+\dfrac{R_L}{R_0+r}} \times \eta_R , \qquad (30)$$

where r is the equivalent resistance (ESR) of a switch, with a constant value for a given switch (e.g., 5.6 mΩ for BSB056N10NN3); R_L is the load resistance at the receiving side; the frequency-dependent resistance R_0 is based on (13); and η_R depicted by (31) is the efficiency of the rectifier at the receiving side [19].
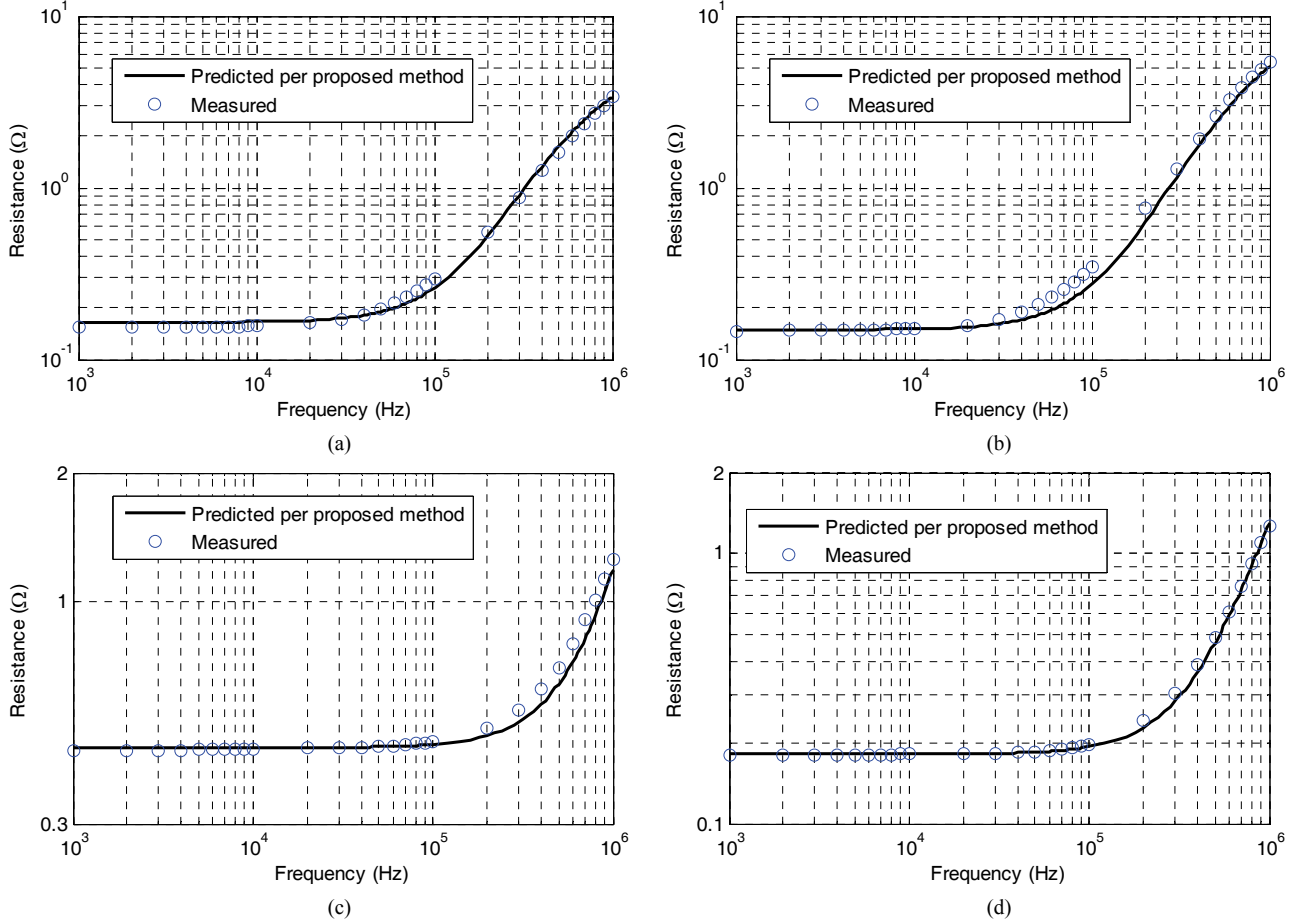
Fig. 6. Predicted and measured resistances of: (a) Coil III, (b) Coil IV, (c) Coil V, (d) Coil VI.

$$\eta_R \approx \frac{1}{1+\dfrac{2V_F}{V_L}}, \qquad (31)$$

where V_F and V_L are the forward voltage and load resistance voltage of the rectifier diode, respectively. The predicted efficiencies for a two-coil WPT are depicted in Fig. 7, where (a) is the surface of the WPT that uses coil IV, (b) is the extracted plot from (a) under load resistances $R_L = 8\,\Omega$ and $R_L = 5.8\,\Omega$, respectively, and (c) denotes the WPT that uses coil II. The coupling inductance $M = 2\,uH$ is adopted in Figs. 7(a) to 7(c), whereas $M = 4\,uH$ is adopted in Fig. 7(d) to depict the influence of coupling inductance on efficiency. The efficiencies are under parameters $V_F = 0.4\,V$ and $V_L = 12\,V$.

For a given load resistance, the predicted efficiency increases with frequency and then decreases after reaching peak efficiency. Peak efficiency occurs at different frequencies under various load resistances. For example, Fig. 7(b) shows that peak efficiency happens at 220 kHz and 260 kHz for $R_L = 5.8\,\Omega$ and $R_L = 8\,\Omega$, respectively, when WPT uses coil IV. When WPT uses coil II, the maximum efficiency under the corresponding load resistances occurs at approximately 0.94 MHz and 1.22 MHz. Another conclusion that can be drawn is that the optimized frequency increases

with load resistance. In addition, a sharper efficiency change occurs closed to the peak efficiency for low load resistances than for high ones, which can be observed from Fig. 7(b), i.e., the plot for $R_L = 5.8\,\Omega$ exhibits a sharper efficiency change at 220 kHz than the plot for $R_L = 8\,\Omega$ at 260 kHz.

Fig. 7 suggests that an appropriate operating frequency for WPT can be selected with given coils and load resistances based on coil AC resistance prediction if efficiency is the key requirement and frequency is not strictly limited. The proposed method can also be used to predict efficiency performance when designing a new coil for WPT.

B. ESR of Resonant Capacitor

The losses disregarded by (30) consist of two parts, namely, the metal-oxide-semiconductor field-effect transistor (MOSFET) switching loss and thermal loss, which result from the capacitor bank ESR. When the switch operates under the zero-voltage switching state, its switching losses are minimal and can be disregarded. The ESR of the resonant capacitor is changeable because various capacitor banks correspond to various operating frequencies, and even the ESR of a given capacitor changes with different frequencies. The ESR of an EPCOS 1nF/2000 v capacitor is measured under various
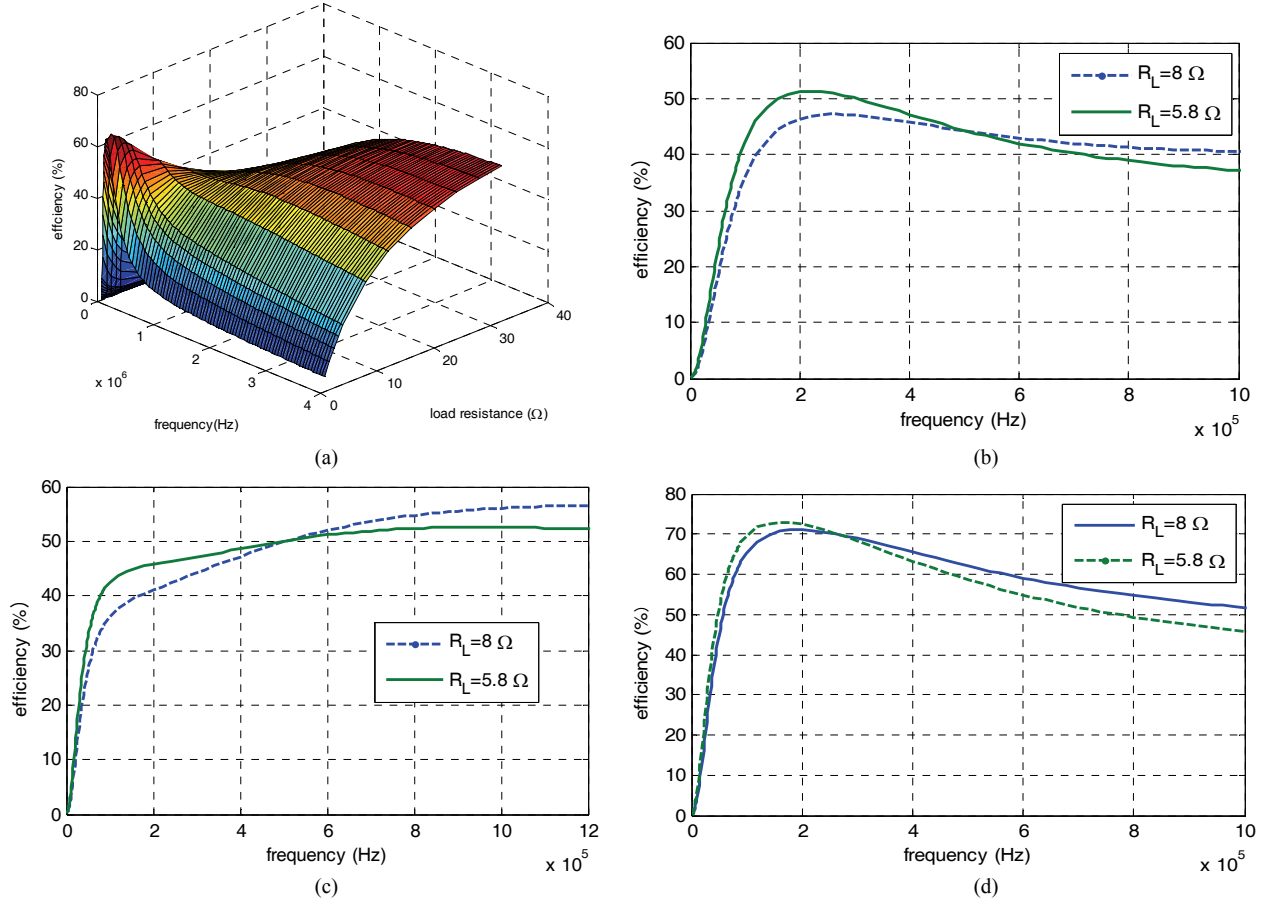
(a)

(b)

(c)

(d)

Fig. 7. Predicted efficiency vs. frequency and resistance under $V_F = 0.4\ V$ and $V_L = 12\ V$.: (a) Surface for WPT that uses coil IV and $M = 2.0\ u$H, (b) Plot for WPT that uses coil IV and $M = 2.0\ u$H, (c) Plot for WPT that uses coil II and $M = 2.0\ u$H, (d) Plot for WPT that uses coil IV and $M = 4.0\ u$H.

frequencies and depicted in Fig. 8(a) with a dashed line. For a series compensation resonant circuit with a given resonant coil, various self-resonant frequencies can be obtained by adjusting the resonant capacitance by

$$C_\omega = \frac{1}{\omega^2 L},\qquad(32)$$

where L and C_ω are the resonant inductance and capacitance of the circuit, respectively. Assume that the resonant capacitor bank is composed of several EPCOS 1 nF/2000 v capacitors connected in parallel. Then, its ESR can be approximately evaluated by

$$r_{C\_bank\_\omega} = \frac{r_{\omega\_1nF}}{10^9 C_\omega}\quad,\qquad(33)$$

where $r_{C\_bank\_\omega}$ and r_{ω_1nF} are the ESR of the capacitor bank with a capacitance C_ω and the ESR of the 1nF capacitor at an angular frequency of ω, respectively.

For example, at a frequency of 50 kHz, the capacitor bank C_ω is 144.7 nF according to (32) under $L = 70\ u$H, which results in an ESR $r_{C\_bank\_\omega}$ of 2.1 mΩ if the capacitor bank is assumed to be composed of 144.7 1nF capacitors connected in parallel, and r_{ω_1nF} is 300 mΩ.

Fig. 8(a) depicts the ESR of capacitor banks according to

(33) under a given resonant inductance of 70 uH at various operating frequencies with a solid line. For comparison, the ESR of the capacitor banks divided by the resistance of coil under various self-resonant frequencies is plotted in Fig. 8(b). The ESR of the capacitor bank accounts for a small proportion of coil resistance. Hence, disregarding the ESR of capacitor banks is reasonable, as shown in (30).

C. WPT Experiment Results

A two-coil WPT system is set up as shown in Fig. 9. Two coils are the same as coil IV, the parameters of which are listed in Table II. A rectifier is connected in series to the receiving loop. The rectifier resistance is 7.25 Ω, which results in a 5.8 Ω ESR in the receiving loop. The half-bridge inverter of the WPT is composed of two BSB056N10NN3 MOSFETs with an on-state resistance of 5.6 mΩ. The rectifier is built with four MBR10100G Schottky barrier rectifier diodes. Different compensated capacitor banks are manufactured to compare efficiency under various frequencies. Several EPCOS 1nF/2000v capacitors are connected in parallel to construct a capacitor bank with a capacitance that is equal to or above 3 nF, whereas combinations of 50, 100, 200, and
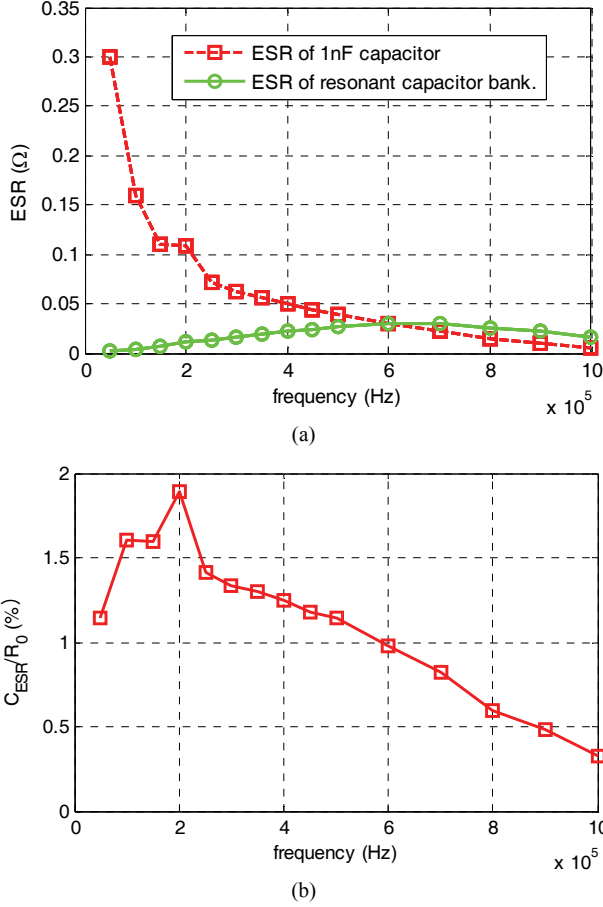
(a)

(b)

Fig. 8. ESR of: (a) 1nF capacitor and various capacitor banks, (b) Capacitor bank divided by the resistance of coil.
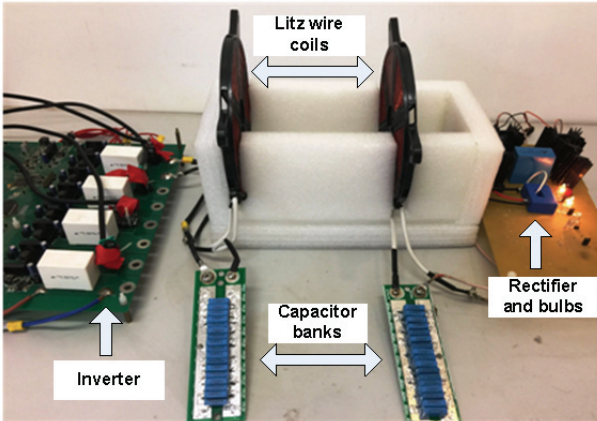

Fig. 9. Two-coil WPT system.

500 pF high-voltage doorknob ceramic capacitors are used to obtain a capacitance below 3 nF. Resistance, coil, and capacitance are measured using an Agilent E4980APrecision LCR meter. The measured ESRs of an EPCOS 1nF/2000 v capacitor are shown in Fig. 8(a). The sending and receiving loops are tuned carefully to the closed self-resonant frequencies. The operating frequencies of the inverter are slightly higher than the corresponding self-resonant frequencies to obtain a
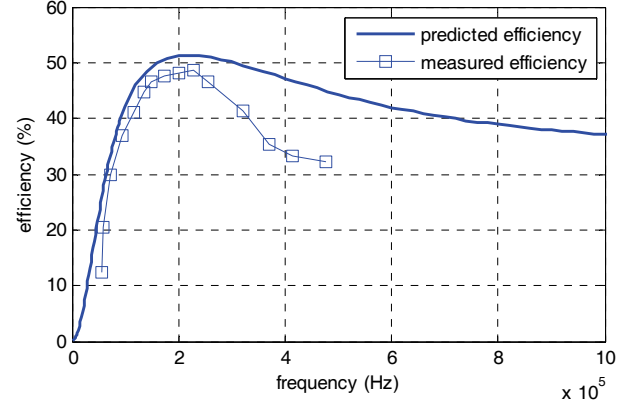

Fig. 10. Efficiency vs. frequency based on (30) at $M = 2.0\ \mu$H and $R_L = 5.8\ \Omega$ for a two-coil WPT that uses coil IV.

zero-voltage switch. The distance between two coils is 156 mm, which provides a coupling inductance of approximately 2 uH via a Maxwell simulation.

For a fair comparison, the input DC voltage at the sending side is regulated to obtain a constant DC voltage at the load resistance, i.e., 12 V for all the experiments. The DC power at both sides, namely, the input DC power of the inverter and the DC power at the load resistance, are measured using two Tektronix PA1000 power analyzers in various experiments. Then, the corresponding efficiencies are calculated based on measured power. Efficiency is defined as the DC power at the load resistance divided by that feeding the inverter.

Fig. 10 shows the predicted and measured efficiencies under typical frequencies. At a frequency range below the optimized frequency for maximum efficiency, the measured efficiencies exhibit an acceptable agreement with the predicted efficiencies.

However, the measured efficiencies decrease faster than the predicted ones at a frequency range above the peak efficiency frequency. In practice, tuning both sides to the same self-resonant frequencies equal to the operating frequency at a high frequency is difficult because a slight parameter deviation results in considerable frequency difference under a small resonant capacitance. Consequently, the output current of the inverter should be increased to obtain a given output power at the load resistance, which considerably reduces efficiency.

Despite these deviations, two plots exhibit the same trend and share nearly the same frequency for maximum efficiencies. This result indicates that the proposed evaluation method for Litz coil AC resistance can help in selecting the optimized operating frequency to obtain maximum efficiency.

VI. CONCLUSIONS

A novel magnetic field evaluation method based on the Biot–Savart law is introduced to analyze the AC resistance of a Litz wire of planar spiral coils. The predicted resistances

based on the proposed method agree well with the measured ones at various frequencies.

For a WPT that uses Litz wire coils, the optimized frequency for the maximum efficiency is changeable with different load resistances and coupling inductances. However, the optimized frequency can be predicted based on the predicted AC resistance of the Litz wire coil from the proposed method. Other conclusions can be drawn based on the Litz wire coil resistance evaluation for a given WPT as follows.

1) The optimized frequency for maximum efficiency increases with the load resistance under given parameter ranges (Fig. 7(a)).

2) A low load resistance indicates rapid efficiency changes around the optimized frequency.

3) Although the proposed method is designed for planar spiral coils, it is applicable to any coils with fields that can be calculated using the Biot–Savart law.

Acknowledgment

References

[1] Y. Zhang, Z. Zhao, and K. Chen, "Frequency decrease analysis of resonant wireless power transfer," *IEEE Trans. Power Electron.*, Vol. 29, No. 3, pp. 1058-1063, Mar. 2014.

[2] J. Acero, R. Alonso, J. M. Burdio, L. A. Barragan, and D. Puyal, "Frequency-dependent resistance in Litz-wire planar windings for domestic induction heating appliances," *IEEE Trans. Power Electron.*, Vol. 21, No. 4, pp. 856-866, Jul. 2006.

[3] C. Carretero, J. Acero, and R. Alonso, "TM-TE decomposition of power losses in multi-stranded Litz-wires used in electronic devices," *Progr. Electromagn. Res.*, Vol. 123, pp. 83-103, Jan. 2012.

[4] J. Acero, P. J. Hernandez, J. M. Burdio, R. Alonso, and L. A. Barragán, "Simple resistance calculation in Litz-wire planar windings for induction cooking appliances," *IEEE Trans. Magn.*, Vol. 41, No. 4, pp.1280-1288, Apr. 2005.

[5] X. Nan and C. R. Sullivan, "An equivalent complex permeability model for Litz-wire windings," *IEEE Trans. Ind. Appl.*, Vol. 45, No. 2, pp. 854-860, Mar. 2009.

[6] X. Nan and C. R. Sullivan, "Simplified high-accuracy calculation of eddy-current loss in round-wire windings," in *Proc. IEEE Power Electron. Spec. Conf. (PESC),* pp. 873-879, 2004.

[7] Z. Pantic and S. Lukic, "Computationally-efficient, generalized expressions for the proximity-effect in multi-layer, multi-turn tubular coils for wireless power transfer systems," *IEEE Trans. Magn.,* Vol. 49, No. 11, pp. 5404-5416, Nov. 2013.

[8] P. L. Dowell, "Effects of eddy currents in transformer windings," *Proc. Inst. Elect. Eng.*, pt. B, Vol. 113, No. 8, pp. 1387-1394, Aug. 1966.

[9] D. Murthy-Bellur, N. Kondrath, and M. K. Kazimierczuk, "Transformer winding loss caused by skin and proximity effects including harmonics in PWM DC-DC flyback converter for continuous conductive mode," *IET Power Electron.*, Vol. 4, No. 4, pp. 363-373, Feb. 2011.

[10] R. P. Wojda and M. K. Kazimierczuk, "Winding resistance of Litz-wire and multi-strand inductors," *IET Power Electron.*, Vol. 5, No. 2, pp. 257-268, Feb. 2012.

[11] C. R. Sullivan, "Optimal choice for number of strands in a litz-wire transformer winding," *IEEE Trans. Power Electron.*, Vol. 14, No. 2, pp. 283-291, Mar. 1999.

[12] F. Tourkhani and P. Viarouge, "Accurate analytical model of winding losses in round Litz-wire windings," *IEEE Trans. Magn.*, Vol. 37, No.1, pp. 538-543, Jan. 2001.

[13] M. Bartoli, N. Noferi, A. Reatti, and M. K. Kazimierczuk, "Modeling Litz-wire winding losses in high-frequency power inductors," in *IEEE Power Electronics Specialists Conf. (PESC) Rec.*, pp. 1690-1696, 1996.

[14] J. Acero, C. Carretero, I. Lope, R. Alonso, and J. M. Burdío, "FEA-bsed model of elliptic coils of square cross section," *IEEE Trans. Magn.*, Vol. 50, No. 7, pp. 1-7, Feb. 2014.

[15] H. Rossmanith, M. Doebroenti, M. Albach, and D. Exner , "Measurement and characterization of high frequency losses in non-ideal Litz-wires," *IEEE Trans. Power Electron.*, Vol. 26, No. 11, pp.3386-3394, Nov. 2011.

[16] A. Rosskopf, E. Bar, and C. Joffe, "Influence of inner skin- and proximity effects on conductive in Litz-wires," *IEEE Trans. Power Electron.*, Vol. 29, No. 10, pp. 5454-5461, Oct. 2006.

[17] S. S. Mohan, M. M. Hershenson, S. P. Boyd, and T. H. Lee, "Simple accurate expressions for planar spiral inductances," *IEEE J. Solid-state Circuits*, Vol. 34, No. 10, pp. 1419-1424, Oct. 1999.

[18] M. Abramowitz and I. A. Stegun, *Handbook of Mathematical Functions*, Dover, 1970.

[19] M. K. Kazimierczuk and D. Czarkowski, "Class D current-driven rectifiers," Ch. 2 in *Resonant Power Converters*, 2nd ed. Wiley-IEEE Press, Hoboken, NJ, 2011.

Xiaona Wang obtained her B.S. in Systems Engineering from Qingdao University of Engineering, Qingdao, China in 1999, her M.Sc. in Systems Engineering from the Naval Aeronautical Engineering Academy, Qingdao, China in 2002, and her Ph.D. in Arms Engineering from the Naval University of Engineering, Wuhan, China in 2008. From 2008 to 2011, she worked as a lecturer in the School of Electrical and Information Engineering, Naval University of Engineering. In September 2011, she joined the School of Electrical Engineering, where she is currently an associate professor. Her research interests include wireless power transfer and electric field protection technology.

Pan Sun obtained his B.S. in Electrical Engineering and Automation and his M.Sc. in Electrical Engineering from the Naval University of Engineering, Wuhan, China in 2009 and 2015, respectively. From 2015 to 2017, he worked as a teaching assistant in the Department of Electrical Engineering, Naval University of Engineering. In December 2017, he joined the Institute of Electrical Engineering, where he is currently a lecturer. His research interests include wireless power transfer, design, and verification of testability.
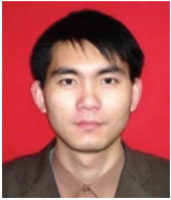
Qijun Deng obtained his B.S. and M.Sc. in Mechanical Engineering from Wuhan University, Wuhan, China in 1999 and 2002, respectively, and his Ph.D. in Computer Application Technology from Wuhan University, Wuhan, China in 2005. In June 2005, he joined the Department of Automation, Wuhan University, where he is currently an associate professor. From 2013 to 2014, he was a visiting scholar in New York University Tandon School of Engineering. His research interests include wireless power transfer, distribution automation, and electrical power informatization.

Wenbin Wang obtained his B.S. from the Wenhua College of Huazhong University of Science and Technology, Wuhan, China in 2008, and his M.Sc. from Wuhan University of Technology, Wuhan, China in 2011. He is currently the head of the New Energy and Microgrid Technology Department of the Distribution Network Technology Center of the State Grid Jiangxi Electric Power Research Institute, which is involved in distributed energy grid testing.